Journal of Alloys and Compounds 674 (2016) 229–244

Contents lists available at ScienceDirect

Journal of Alloys and Compounds

journal homepage: http://www.elsevier.com/locate/jalcom

Full Length Article

Oxidation behavior of arc melted AlCoCrFeNi multi-component high-entropy alloys

Todd M. Butler*, Mark L. Weaver

Department of Metallurgical and Materials Engineering, Box 870202, University of Alabama, Tuscaloosa, AL 35487-0202, USA

ARTICLE INFO

Article history:
Received 1 December 2015
Received in revised form
31 January 2016
Accepted 29 February 2016
Available online 2 March 2016

Keywords:
High-entropy
Oxidation
Multi-component
Alumina-former

ABSTRACT

Multi-component, high-entropy alloys (HEAs) are being investigated as potential alternatives for high temperature structural materials due to their reported high symmetry crystal structures, favorable mechanical properties, high temperature phase stabilities, and resistances to degradation in oxidizing/corrosive environments. However, their high temperature oxidation behaviors are poorly understood. In this work, the as-cast microstructures and 1050 °C oxidation behaviors of a series of arc-melted $Al_x(NiCoCrFe)_{100-x}$ HEAs where x = 8, 10, 12, 15, 20, and 30 (at.%) were investigated. The dominant structure of the low Al concentration HEAs was determined to be FCC, while the high Al concentration HEAs were BCC dominant. A structural transition point at ~15 at. % Al exists where a large fraction of both FCC and BCC are present. Each HEA exhibited initial transient oxidation followed by various degrees of parabolic oxide growth. All of the HEAs formed a combination of Al_2O_3 and AlN beneath an external Cr_2O_3 scale. Increased Al content improved the continuity and internal position of the Al_2O_3 scale, resulting in enhanced oxidation resistances. These results are discussed relative to chemically similar conventional alloys and existing Ni–Cr–Al oxide formation models. The resulting phase equilibria has been compared to thermodynamic predictions made using the CALPHAD method.

1. Introduction

Multi-component high entropy alloys (HEAs), also known as compositionally complex alloys, are receiving significant interest in the materials engineering community due to their unique microstructures and reportedly enhanced thermal, mechanical, and corrosive properties [1–7]. Unlike conventional alloys, HEAs are comprised of five or more components in nearly equal proportions. This broad definition is often coupled with the entropy constraint of $\Delta s_{mix} \geq 1.5R$, where Δs_{mix} is the calculated ideal configurational entropy of mixing and R is the ideal gas constant [1]. The ideal configurational entropy of mixing depends only on the concentration of each element in the alloy and is classically defined by Refs. [2–4]:

$$\Delta s_{mix} = -R\sum_{i=1}^{n} c_i \ln(c_i) \quad (1)$$

where C_i is the concentration of component i. For equiatomic HEAs, this term is simplified and is defined by:

$$\Delta s_{mix} = R\ln(N) \quad (2)$$

where N is the number of components in the alloy. These chemical arrangements have been shown to facilitate the retention of high-entropy, solid solution BCC and/or FCC type crystal structures upon cooling. However, in many HEA systems, the formation of a combination of solid solution and intermetallic phases are observed. The valence electron concentration (VEC) is another factor used to describe HEAs and is relevant to this investigation. The VEC is defined by Refs. [2,3,5]:

$$VEC = \sum_{i=1}^{n} c_i (VEC)_i \quad (3)$$

where the VEC is the average VEC considering all elements and their respective concentrations. This term is useful in predicting the crystal structures of the phases that form in HEAs. For example, alloys with VEC values greater than 8 have been found to stabilize FCC type phases, while alloys with VEC values below ~6.87 stabilize

* Corresponding author.
E-mail address: tmbutler@crimson.ua.edu (T.M. Butler).

http://dx.doi.org/10.1016/j.jallcom.2016.02.257
0925-8388/

BCC structures [3,6]. Similarly, alloys with mid-range VECs are expected to form a combination of FCC and BCC type phases. In the widely studied AlCoCrFeNi-based HEAs, it is also known that increasing the relative concentrations of Co and Ni tends to stabilize FCC type phases whereas increased Al and or the addition of Ti tends to stabilize BCC and/or B2 type phases with concomitant changes in properties and performance.

The potential for the use of HEAs in high-temperature applications is immense, yet an understanding of their oxidation behaviors and the development of effective models to predict their behaviors are lacking. With regard to oxidation, HEAs are less compositionally constrained than conventional structural alloys (e.g. stainless steels, Ni-based superalloys) because they can accommodate higher concentrations of the elements that are necessary to form protective external oxide scales (e.g., Al and/or Cr) [7]. Furthermore, HEAs have also been reported to exhibit sluggish diffusion kinetics [5,8–10], which could enhance their oxidation behaviors by inhibiting the formation of non-protective transient oxides. This could also have a beneficial impact on the long term microstructural stability of HEAs exposed to high temperature environments.

With that in mind, there have been several investigations of the oxidation behaviors of a variety of different HEAs [11–29]. The reported results indicate that in many cases HEAs, like more conventional alloys, tend to selectively oxidize and exhibit varying modes of oxide growth. However, no reported works attempt to directly correlate the active oxide formation mechanisms in HEAs to existing oxide formation models derived from model alloys containing like elements.

The present study has been conducted to elucidate the microstructures and mechanisms of oxidation in a series of AlNiCoCrFe based HEAs. This document which focuses on arc-melted HEAs represents the first part of a systematic study of the fundamental oxidation behaviors of HEAs. Similar observations for annealed alloys will be the subject of another paper. The results have been compared to relevant conventional alloys and existing oxide formation models in order to help facilitate in the design of future oxidation resistant HEAs. Additionally, the experimental observations have been compared with those predicted using thermodynamic models to assess the merit and validity of existing thermodynamic databases.

2. Material and methods

Bulk alloys with the compositions of $Al_x(NiCrCoFe)_{100-x}$, where x = 8, 10, 12, 15, 20, and 30 at.% (designated: Al_8, Al_{10}, Al_{12}, Al_{15}, Al_{20}, Al_{30}) were synthesized into buttons via arc-melting pure constituents (purity > 99.9%) on a water-cooled copper hearth under an inert argon atmosphere. Each button was flipped and re-melted multiple times to promote homogeneity. The overall alloy compositions (nominal and experimental), as determined using energy-dispersive x-ray spectroscopy (EDS), are shown in Table 1.

The HEAs were investigated using a combination of scanning electron microscopy (SEM), EDS, transmission electron microscopy (TEM), and x-ray diffraction (XRD). EDS was performed in both SEM and TEM modes. Specimens for TEM analysis were made using a variation of the focused-ion-beam (FIB) in situ lift-out method for TEM foil preparation in an FEI Quanta 200 3D Dual Beam FIB-SEM [30]. Plan view and cross-sectional images of the as-cast and oxidized HEAs were captured on a JEOL 7000F SEM in back-scattered (BSE) and secondary electron modes (SE). High angle annular dark field (STEM-HAADF) images and selected area diffraction patterns (SADPs) were captured on a 200-KeV FEI Tecnai G^2 F-20 Supertwin scanning-transmission electron microscope (S) TEM. TEM–EDS data was evaluated using FEI ES Vision software with an applied thickness correction [31]. XRD spectra were collected from bulk samples using a Philips X'pert MPD XRD with Cu-Kα radiation at 45 kV and 40 mA. Volume fraction calculations were done using ImageJ software. The area fraction of each phase was used to determine an equivalent volume fraction.

Discontinuous, isothermal oxidation of the as-cast HEAs was conducted at 1050 °C under ambient laboratory air in a Thermoline 1100 tube furnace. Tests were carried out to 100 h. Before the oxidation tests, specimens were ground to a 1200 grit surface finish using SiC paper, cleaned with acetone/isopropanol, and placed into annealed alumina boats. Samples were removed from the furnace periodically in order to record their relative mass changes and to investigate their structural evolution via XRD. Mass measurements were conducted using an Orion Cahn C-34 microbalance (1×10^{-6} g sensitivity). Phase equilibria has been simulated using the CALPHAD method in the ThermoCalc™ software package using the TCNI8 (Ni-based superalloys) database [32–34].

3. Results and discussion

3.1. Introduction

The components used to fabricate the HEAs examined in this study were limited to Al, Co, Cr, Fe, and Ni in order to provide a model HEA system that could be compared to conventional structural materials composed of similar constituents (e.g., steels and M–Cr–Al alloys). Using the expanded classification scheme recommended by Miracle et al. [1], all of the alloys in this study exhibit "high-entropy" character, as is evident from the calculated ideal entropy of mixing values of >12.47 in Table 1.

3.2. Microstructures of the as-cast alloys

Fig. 1 shows representative SEM images for each of the studied HEAs in their as-cast states. The low Al concentration HEAs (Al_8, Al_{10}, and Al_{12}) (Fig. 1 (a) – (c)), were composed of medium atomic number contrast (i.e., medium-Z) dendrites (D) interspersed with lower-Z contrast interdentritic (ID) regions. The dendrites were found to have compositions that were close to the nominal alloy compositions (Table 1), while the ID regions were found to be Ni and Al rich. When imaged at higher magnifications, the ID regions were found to consist of a mixture of two phases; a semi-continuous low-Z contrast matrix phase intermixed with fine-scale, high-Z precipitates (inset images in Fig. 1 (a)-(c)). The observed dendritic solidification structures are analogous to those reported in other AlNiCoCrFe-based and AlCoCrCuFeNi HEAs [35–43].

To examine these microstructures further, TEM analysis was done on the Al_{10} and Al_{12} HEAs, Figs. 2 and 3. Fig. 2 (a)-(c) show a mosaic STEM-HAADF image and SADPs collected from the Al_{10} HEA. The D regions in this HEA were found to have a disordered FCC structure (a_{FCC} = 3.599 Å) and to be enriched in Cr, Fe, and Co (Table 1). In contrast, the ID regions consisted of a B2 matrix (a_{B2} = 2.875 Å) that was enriched in Ni and Al and encompassed Cr-rich BCC precipitates. The BCC and B2 phases were found to be fully coherent, exhibiting a cube-on-cube orientation relationship and indistinguishable lattice parameters. A similar distribution of phases with comparable lattice parameters (a_{FCC} = 3.532 Å and a_{B2} = 2.879 Å) was observed in the Al_{12} HEA, Fig. 3 (a)-(d). Although TEM was not performed on the Al_8 HEA, it is likely that a comparable allotment of phases exists based on the microstructural and chemical information obtained via SEM. These phase structures are consistent with the work of Wang et al. [37], who reported similar microstructures in chemically analogous HEAs. Similar phase distributions have also been reported in AlCoCrCuFeNi HEAs [40–43]. However, the additional presence of Cu in this system promotes

Table 1
Chemical compositions of the as-cast HEAs and individual phase compositions as determined by EDS (at.%). The determined lattice parameters for the phases are shown along with the entropy of mixing and the VEC for each HEA.

Alloy	Phase	Crystal structure	Al	Cr	Fe	Co	Ni	Lattice Parameter (a)	ΔS_{mix} (J/mole × K)	VEC
Al_8	Overall	–	8.2 ± 0.2	24.0 ± 0.3	22.8 ± 0.2	22.8 ± 0.2	22.2 ± 0.5	–	12.94	7.78
	D	FCC	10.4 ± 0.2	25.1 ± 0.1	20.3 ± 0.4	20.8 ± 0.2	23.4 ± 0.1	3.545 Å	–	–
	ID – matrix	B2	22.5 ± 0.1	18.6 ± 0.4	13.9 ± 0.1	16.4 ± 0.1	28.6 ± 0.4	–	–	–
	ID – Ppt.	BCC	17.1 ± 0.5	26.7 ± 1.1	16.5 ± 0.6	16.8 ± 0.4	22.9 ± 0.8	–	–	–
Al_{10}	Overall	–	10.2 ± 0.1	22.6 ± 0.2	21.8 ± 0.1	21.7 ± 0.08	23.6 ± 0.2	–	13.08	7.73
	D	FCC	9.5 ± 0.6	22.8 ± 0.1	22.5 ± 0.7	22.1 ± 0.5	23.2 ± 0.6	3.599 Å	–	–
	ID - matrix	B2	25.5 ± 0.5	7.1 ± 1.9	11.4 ± 1.1	16.6 ± 0.9	39.5 ± 1.6	2.875 Å	–	–
	ID – Ppt.	BCC	13.4 ± 0.1	28.1 ± 0.2	13.7 ± 1.1	17.7 ± 1.1	27.2 ± 0.2	–	–	–
Al_{12}	Overall	–	12.1 ± 0.1	21.9 ± 0.1	21.8 ± 0.6	21.7 ± 0.6	22.5 ± 0.6	–	13.20	7.62
	D	FCC	11.2 ± 0.1	23.9 ± 0.1	19.2 ± 0.4	20.2 ± 0.3	25.4 ± 0.5	3.532 Å	–	–
	ID - matrix	B2	27.4 ± 3.2	6.4 ± 1.6	10.3 ± 0.9	16.2 ± 0.9	39.7 ± 0.3	2.879 Å	–	–
	ID – Ppt.	BCC	21.0 ± 1.7	21.7 ± 1.9	14.7 ± 0.8	16.5 ± 0.4	26.1 ± 1.5	–	–	–
Al_{15}	Overall	–	15.6 ± 0.1	21.9 ± 0.1	21.1 ± 0.1	20.8 ± 0.1	20.5 ± 0.1	–	13.33	7.40
	D	FCC	12.6 ± 0.7	21.8 ± 0.7	21.7 ± 0.1	21.5 ± 0.7	21.4 ± 0.7	3.674 Å		
	ID – Matrix	BCC	5.5 ± 1.3	30.8 ± 0.9	21.4 ± 2.0	21.1 ± 0.3	21.3 ± 3.9	–	–	–
	ID – Ppt.	B2	19.7 ± 1.9	11.2 ± 3.6	16.5 ± 1.5	21.5 ± 0.7	31.3 ± 3.6	2.890 Å	–	–
Al_{20}	Overall	–	20.2 ± 0.1	20.8 ± 0.2	20.1 ± 0.1	19.7 ± 0.1	19.3 ± 0.1	–	13.38	7.12
	Ppt.	BCC	17.1 ± 0.9	29.5 ± 2.4	23.8 ± 1.0	15.9 ± 0.9	13.7 ± 3.4	–	–	–
	Matrix	B2	32.2 ± 1.2	5.1 ± 0.2	12.8 ± 1.8	24.3 ± 0.4	25.6 ± 0.1	2.819 Å	–	–
Al_{30}	Overall	–	29.2 ± 0.2	18.3 ± 0.1	17.6 ± 0.2	17.6 ± 0.1	17.4 ± 0.1	–	13.18	6.70
	Ppt.	BCC	17.2 ± 0.5	29.3 ± 2.2	24.1 ± 1.7	16.3 ± 1.9	13.2 ± 1.4	–	–	–
	Matrix	B2	32.2 ± 0.7	4.6 ± 0.4	13.1 ± 0.1	24.1 ± 0.7	25.9 ± 0.2	2.822 Å	–	–

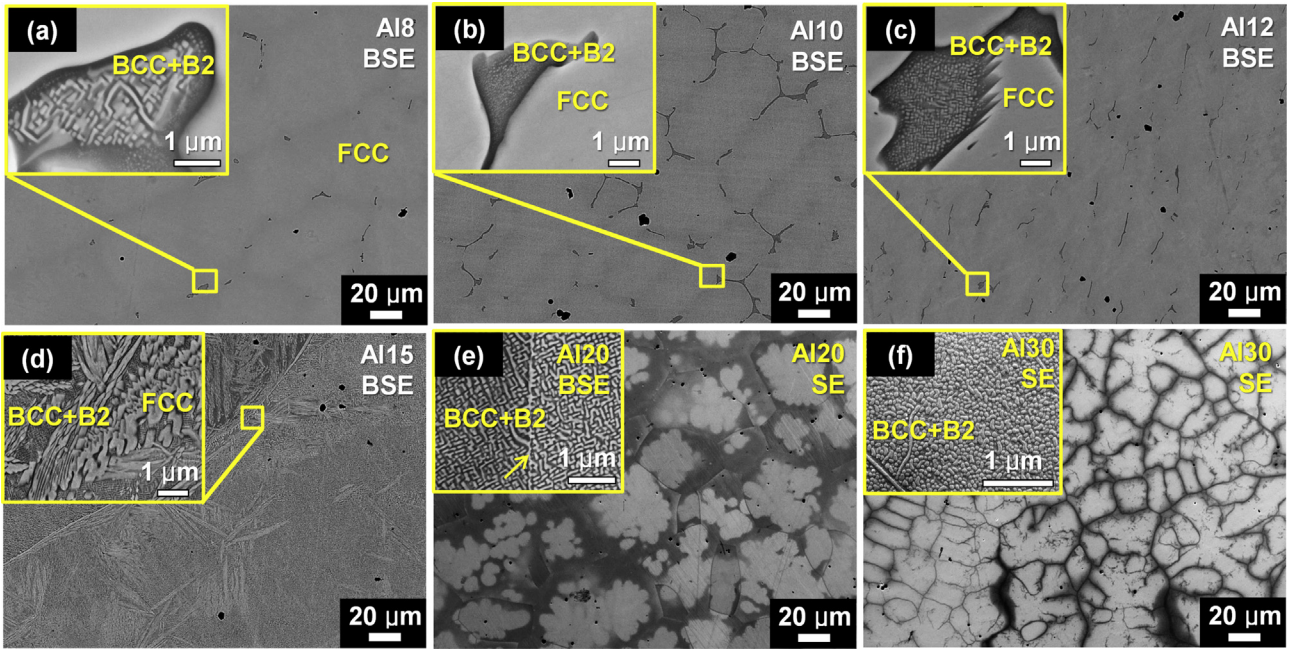

Fig. 1. Representative BSE and SE micrographs of the as-cast Al_8 (a), Al_{10} (b), Al_{12} (c), Al_{15} (d), Al_{20} (e), and Al_{30} (f) HEAs in this study.

other Cu-rich FCC precipitate phases that were not observed in this work. All of the alloys contained less than 1 vol. % AlN inclusions which could be attributed to impurities in the starting materials.

The Al_{15} HEA exhibited a coarse multi-phase microstructure consisting of high-Z contrast Widmanstätten-like lamellae interspersed with highly transformed regions exhibiting a modulated two-phase microstructure that was reminiscent of the ID regions in the Al_8, Al_{10}, and Al_{12} HEAs, Fig. 1 (d). TEM analysis showed the high-Z contrast lamellae to have an FCC crystal structure (a_{FCC} = 3.674 Å), whereas the transformed regions consisted of a high-Z BCC matrix intermixed with low-Z B2 precipitates (a_{B2} = 2.890 Å), Fig. 4 (a)-(c). Chemically, the FCC phase in the Al_{15} HEA was lean in Ni and Al and was similar to the ones found in the lower Al content HEAs, Table 1. The B2 phase in the transformed regions was enriched in Ni and Al, while the BCC phase was rich in Cr, Table 1. These observations are consistent with the work of Tong et al. [43] who reported a combination of FCC and BCC type phase structures in AlCoCrCuFeNi HEAs with moderate concentrations of Al. With regard to chemistries, it was also reported that Ni and Al tended to segregate to ordered B2 regions, while Fe, Co, and Cr segregated to disordered regions.

Fig. 1 (e) and (f) show the microstructures observed in the higher Al concentration HEAs (Al_{20} and Al_{30}). Both HEAs exhibited a fine-scale Cr-rich precipitation product within individual grains along with a semi-continuous layer of the same phase along the grain boundaries (this is noted with an arrow in Fig. 1 (e)). The

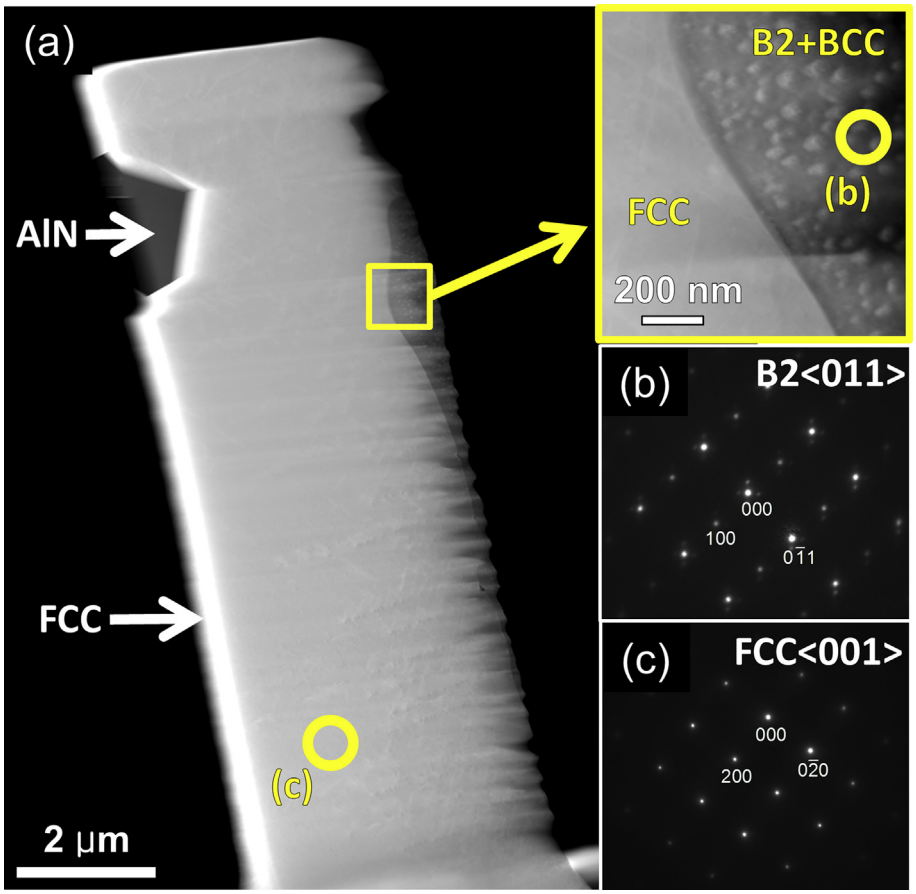

Fig. 2. Microstructure of the as-cast Al_{10} HEA: Mosaic STEM-HAADF image of the specimen lifted out across an interdendritic region (a), and corresponding SADPs (b)–(c). The enclosed circles represent where the SADPs were captured from for each phase.

microstructures closely resembled coarsened versions of the modulated BCC + B2 microstructures observed in the lower Al concentration HEAs, Fig. 1 (a)-(d). TEM analysis of both HEAs (Figs. 5 and 6) showed the entire microstructures to consist of a fine-scale distribution of BCC precipitates in a B2 matrix ($a_{B2} = 2.819$ Å). Comparable microstructures have been observed in high Al content AlNiCoCrFe and AlNiCoCrFeCu HEAs [40–43]. In the latter, it has been proposed that the modulated BCC + B2 microstructures form via a spinodal decomposition reaction [42,43]. As was noted previously in the low Al content HEAs, the B2 matrix phase was rich in Ni and Al, while the BCC phase was rich in Cr, Table 1.

The general structure evolution with increased Al content was investigated via XRD. Fig. 7(a) shows XRD spectra from the as-cast HEAs in this study. Consistent with the SEM and TEM observations, the lower Al content HEAs (i.e., Al < 15 at.%) exhibited FCC dominant microstructures. Likewise, the high Al content HEAs (i.e., Al > 15 at.%) exhibited BCC dominant microstructures. The Al_{15} HEA appeared to sit at a transition point between the two, exhibiting both FCC and BCC-type (i.e., BCC and/or B2) phases, consistent with the large volume fraction of BCC, B2 and FCC phases observed via TEM, Fig. 4. This general trend is consistent with the XRD results of Wang et al. [37] on comparable as-cast HEAs. In addition, the AlNiCoCrFeCu system tends to follow a similar structural transition with increased Al content [43].

This structural transition was explored further through comparison with the VEC value for each HEA. The calculated VECs for each as-cast HEA are shown in Table 1. As mentioned previously, HEAs exhibiting VECs in excess of ~8 tend to stabilize FCC type phases, while VEC values below ~6.87 tend to stabilize BCC-type structures [3,6]. Likewise, VECs in between these two boundaries stabilize a combination of FCC and BCC-type phases. These boundaries are plotted with the respective VECs for the HEAs in this study in Fig. 7 (b). All of the HEAs, aside from the Al_{30} fall in the region that predicts a combination of BCC and FCC phases. However, the microstructural analysis in this work shows that these predictions are inconsistent with experimental results. The Al_{20} HEA, which sits well within the predicted FCC + BCC predicted region was actually found to contain only BCC and B2 phases. This infers that the prediction ranges based on VECs for AlCoCrFeNi HEAs may need to be refined. However, it is important to remember that the microstructural observations are based solely on non-equilibrium, as-cast alloys, which could explain the discrepancy for the Al_{20} HEA. The VEC prediction does also match the relative phase fraction of BCC-type phases in the Al_8–Al_{15} HEAs. Nearing the FCC boundary promotes a higher amount of stabilized FCC phase, while moving toward the BCC boundary facilitates a higher fraction of BCC type phases. This idea is consistent with the experimental observations.

3.3. Thermodynamic modeling of the as-cast HEAs

There have been several studies of HEAs that have attempted to utilize thermodynamic models to predict phase formation as a function of alloy composition [44–47]. In all of these studies, the thermodynamic models were compared with experiments to

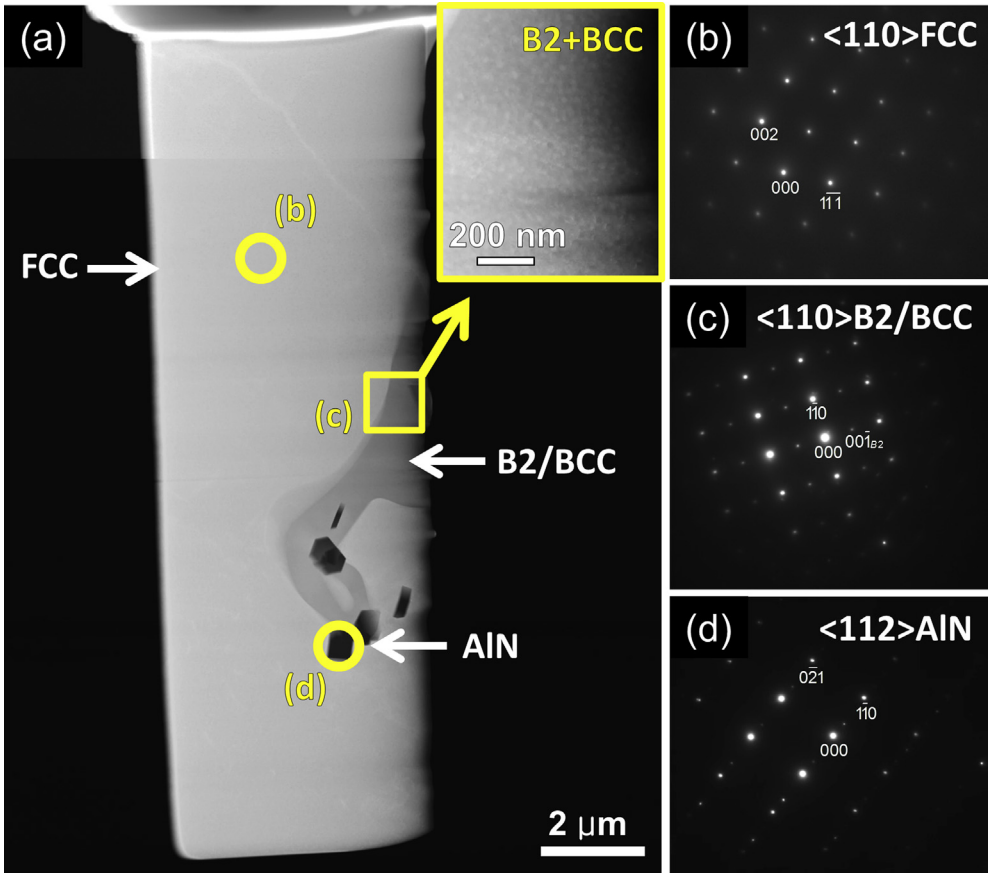

Fig. 3. Microstructure of the as-cast Al_{12} HEA: Mosaic STEM-HAADF image of the specimen lifted out across an interdendritic region (a), and corresponding SADPs (b)–(d). The enclosed circles represent where the SADPs were captured from for each phase.

validate their effectiveness. The majority of these simulations use the CALPHAD method. The CALPHAD method assumes that equilibrium corresponds to a state of minimum Gibbs free energy of the system, whereby the most probable/stable phases exhibit the lowest Gibbs free energies. For this study, equilibrium predictions in five element space were derived from extrapolations of experimentally backed binary and ternary systems.

Fig. 8 shows the phase diagrams for each HEA as calculated using Thermo-Calc. The calculations were based on the experimentally determined bulk compositions indicated in Table 1. The stable phases predicted over a range of temperatures (200–1500 °C) in the low Al content alloys (≤15 at.%) were FCC, BCC, B2, $L1_2$, sigma, and liquid, Fig. 8 (a)-(d). For the high Al content alloys, the predicted stable phases include B2, BCC, sigma, and liquid, Fig. 8 (e)-(f). The sigma phase and $L1_2$ phase were not experimentally observed in any of the HEAs. However, the thermodynamic predictions suggest that both phases are only stable at low to intermediate temperatures (~100 °C–800 °C), Fig. 8. Due to the slow diffusion kinetics of HEAs, it is plausible to suggest that the sigma and $L1_2$ phases might not form during cooling but would form after aging in their stable temperature ranges.

In general, the microstructural findings for the arc-melted HEAs in this study correlated well with the high temperature phase predictions. Considering temperatures slightly above 1000 °C, all of the HEAs were predicted to be multi-phase, Fig. 8. In particular, the Al_8–Al_{15} HEAs show predicted high temperature microstructures consisting of a combination of FCC and B2 phases, Fig. 8 (a)-(d). The high Al content HEAs were predicted to contain BCC and B2 phases, Fig. 8 (e)-(f). These predictions are consistent with the experimental observations, Figs. 2–6. It is important to note that the thermodynamically predicted trend in the amount of FCC versus BCC type phases with varied alloy chemistry also corroborates with the experimental findings. Additionally, the transformation from an FCC dominant microstructure to a BCC dominant microstructure was captured in the thermodynamic simulations, Fig. 8. As the Al concentration is increased, the volume fraction of BCC/B2 phases increases proportionally. Upon reaching 15 at.% Al, the microstructure is predicted to contain near-equal amounts of FCC and B2 phases. Upon exceeding 15 at.% Al, the FCC phase is no longer predicted, leaving a microstructure consisting entirely of BCC and B2 phases. These observations show the merit and usefulness of thermodynamic models for predicting the phases that form in as-cast HEAs. It is expected that with proper annealing treatments, the models would correlate with the resulting microstructures.

3.4. Oxidized microstructures

Figs. 9–14 show representative post oxidation microstructures for the HEAs after 50 h of oxidation in air at 1050 °C. Based on BSE observations, the Al_8 and Al_{10} HEAs formed an external Cr_2O_3 scale above an internal, discontinuous Al_2O_3 scale (Fig. 9 (a)-(b) and 10 (a)-(b), respectively). Some AlN precipitates were observed just beneath the Al_2O_3 layer. Krupp and Christ [48] reported a similar formation of nitrides during the oxidation of single crystal Ni-based superalloys. These post oxidation microstructures are comparable to the work of Zhang et al. [13] who studied the 900 °C oxidation behaviors of $Al_{0.5}FeCoCrNi$ and $Al_{0.5}CoCrFeNiSi_{0.2}$ HEAs in air and

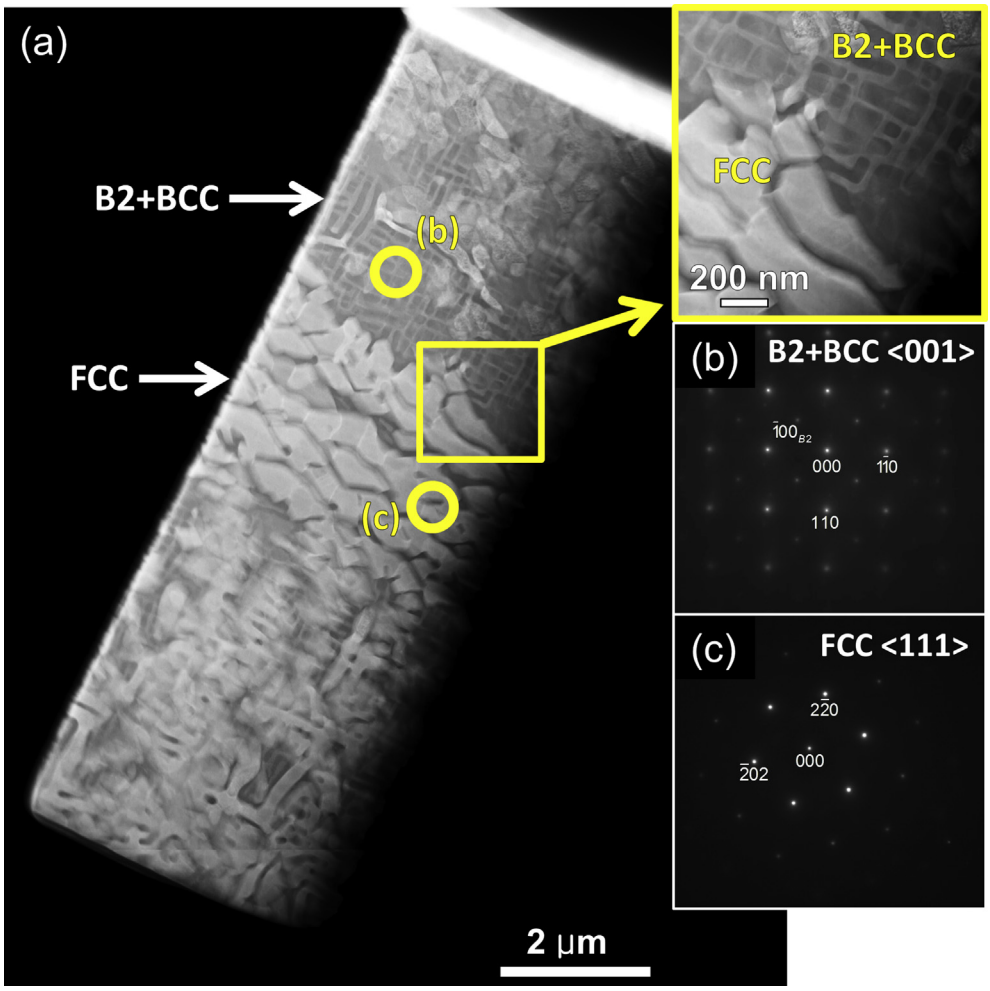

Fig. 4. Microstructure of the as-cast Al_{15} HEA: Mosaic STEM-HAADF image of the specimen lifted out across a phase boundary (a) and corresponding SADPs (b)–(c). The enclosed circles represent where the SADPs were captured from for each phase.

Hall et el [49]. who investigated the oxidation behavior of model FeNiCrAl alloys at 900 °C. The Al_8 and Al_{10} HEAs also exhibited a thin sub-layer of metal between the Cr_2O_3 and Al_2O_3 scales that was enriched in oxygen. In both HEAs, the internal interdendritic regions tended to decompose into smaller low-Z clusters and platelets, as is shown by the BSE images in Fig. 9 (c) and 10 (c). These low-Z regions were still rich in Ni and Al, while the internal matrix was enriched in Cr, Fe, and Co, as shown in Table 2. As expected, both HEAs exhibited Al depleted zones near the surface, Table 2.

To investigate the phase crystal structures in the Al_8 and Al_{10} HEAs, TEM analysis was conducted. Specimens were lifted out perpendicular to the oxide surface in order to capture all of the phases near the surface. Fig. 9 (d)-(h) and 10 (d)-(h) show mosaic STEM-HAADF images and SADPs from the oxidized Al_8 and Al_{10} HEAs. Consistent with SEM observations, the oxidized Al_8 and Al_{10} HEAs consisted of an outer Cr_2O_3 scale, an internal oxygen-enriched metal sub-layer, a discontinuous internal Al_2O_3 scale, and AlN precipitates. The depleted zones for the Al_8 and Al_{10} HEAs were found to have FCC structures, as is evident from the SADPs in Figs. 9 and 10, respectively.

The oxidized Al_{12} and Al_{15} HEAs, Figs. 11 and 12, formed an external layer of Cr_2O_3 along with a discontinuous, internal Al_2O_3 scale. Like the Al_8 and Al_{10} HEAs, AlN precipitates were also found beneath the Al_2O_3. The increased Al content improved the continuity of the Al_2O_3 scales in both HEAs and eliminated the oxygen-enriched metal sub-layer under the outer Cr_2O_3 scale, Fig. 11 (b) and 12 (b). In contrast to the Al_8 and Al_{10} HEAs, the Al_{12} and Al_{15} HEAs also formed an external $NiCr_2O_4$ spinel. This spinel phase was not observed in all of the HEAs, but these phases commonly form during the initial stages of oxidation in Ni–Cr–Al type alloys [50]. Internally, the Ni and Al-rich interdendritic regions in the Al_{12} HEA decomposed in a fashion similar to the Al_8 and Al_{10} HEAs, Fig. 11 (c). The platelets were still enriched in Ni and Al, while the matrix contained higher amounts of Cr, Co, and Fe, Table 2. The Al_{12} HEA also exhibited an Al depleted zone that was virtually identical, chemically, to the depleted zone in the Al_{10} HEA. As for the internal microstructure of the oxidized Al_{15} HEA, a coarsened combination of high-Z and low-Z phases was observed, Fig. 12 (c). Compositionally, the high-Z phase was enriched in Cr, Fe, and Co, while the low-Z phase was rich in Ni and Al, Table 2.

TEM analysis was also conducted on the Al_{12} and Al_{15} HEAs, as shown by the mosaic STEM-HAADF images and SADPs in Fig. 11 (d)-(h) and 12 (d)-(h), respectively. Consistent with SEM findings, these HEAs formed an outer $NiCr_2O_4$ spinel on top of a continuous Cr_2O_3 scale, with an underlying mixture of semi-continuous Al_2O_3 and AlN precipitates. Much like the Al_8 and Al_{10} HEAs, Al-depleted zones with FCC structures were observed in both HEAs. The Al_2O_3 scales also formed directly beneath the Cr_2O_3, rather than below an

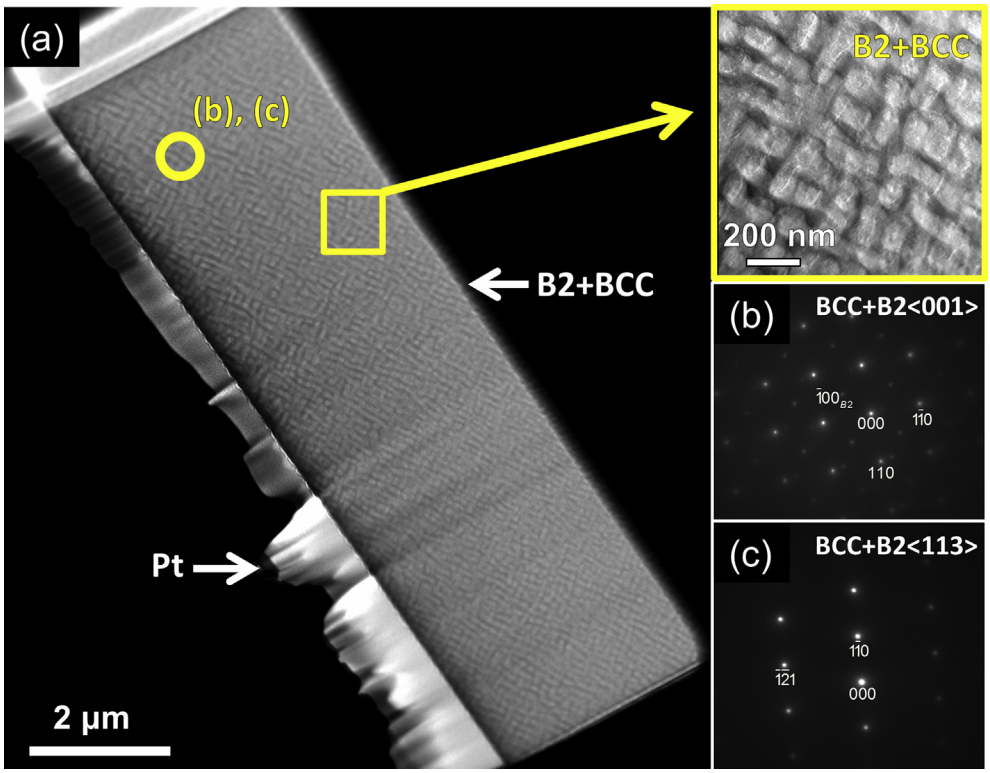

Fig. 5. Microstructure of the as-cast Al_{20} HEA: Mosaic STEM-HAADF image of the specimen lifted out from a grain interior (a), and corresponding SADPs (b)–(c). The enclosed circles represent where the SADPs were captured from for each phase.

internal oxygen-enriched metal sub-layer. The formation of a more continuous Al_2O_3 layer is known to enhance the oxidation resistances in Ni–Cr–Al alloys [50].

The oxidized Al_{20} and Al_{30} HEAs formed external Cr_2O_3 scales on top of continuous internal Al_2O_3 scales (Figs. 13 and 14, respectively). These high Al content HEAs also displayed fewer AlN precipitates beneath the Al_2O_3 scale, Fig. 13 (b) and 14 (b). Qualitatively, both HEAs formed thicker layers of Al_2O_3 and thinner layers of Cr_2O_3 in comparison to the lower Al content HEAs. For the Al_{30} HEA, some regions of bare metal were observed in plan-view, indicating some degree of oxide spallation and/or volatilization, Fig. 14 (a). Internally, the Al_{20} and Al_{30} HEAs both exhibited a continuous low-Z matrix enriched in Ni and Al, with a Cr-rich, high-Z phase on the grain boundaries and internally within grains, Fig. 13 (c) and 14 (c) and Table 2.

TEM analysis was conducted on the oxidized Al_{20} and Al_{30} HEAs, as shown by the mosaic STEM-HAADF images and SADPs in Fig. 13 (d)-(h) and 14 (d)-(i). Consistent with SEM results, the oxidized Al_{20} HEA formed an outer oxide scale of Cr_2O_3 on top of a continuous internal sub-layer of Al_2O_3, along with several AlN precipitates, Fig. 13 (d). The depleted zone below the oxide scales was found to have a BCC structure. Similarly, the Al_{30} HEA contained the same arrangement of phases, Fig. 14. However, the depleted zone was found to consist of a mixture of regions containing B2 precipitates in a BCC matrix or uniform B2 regions, Fig. 14 (d). As discussed previously, the Al_{20} and Al_{30} HEAs displayed thinner outer Cr_2O_3 scales and thicker, more continuous Al_2O_3 scales.

The phases identified via SEM and TEM in the 50 h oxidized HEAs were verified using XRD, as shown in Fig. 15. Patterns were captured in plan-view from bulk oxidized samples. As expected, XRD peaks corresponding to a combination of FCC, BCC, B2, Al_2O_3, Cr_2O_3, AlN, and $NiCr_2O_4$ phases were observed. This validates the experimental results obtained from electron microscopy.

3.5. Oxidation behavior

Fig. 16 (a) shows the mass change per unit area as a function of oxidation exposure time at 1050 °C. There was a clearly observed dependence of Al concentration on the relative oxidation resistances. Each alloy exhibited mass gains with initial transient oxidation (typically 1–2 h in duration), followed by various degrees of steady-state parabolic oxide growth. For the highest Al content HEAs, the curves tended to statistically plateau after about 10–30 h of oxidation, suggesting a combination of spallation or volatilization followed by self-healing [51]. The mass changes in all cases were comparable to those observed for Ni–Cr–Al alloys, FeCoNi-based equi-molar alloys, and several wrought nickel-based superalloys [52–57]. The parabolic oxide growth rate constants (k_p) calculated from the slopes of $(\Delta W/A)^2$ versus t plots for each alloy are shown in Table 3, along with the adherence times and primary observed oxides. For the instances where multiple stages of oxidation were observed, several k_p values were calculated.

In general, the increased Al content expedited the initial stages of transient oxidation and initiated an earlier state of passivation, Fig. 16 (a). This earlier protective state for the high Al content HEAs led to lower total mass changes for the entire duration of oxidation testing. As expected, increased Al content resulted in better oxidation resistances. Interestingly, the Al_{15} HEA was observed to be the chemical transition point where the initial stages of oxidation began to accelerate, facilitating earlier steady-state oxidation, Fig. 16 (a). The high mass change observed for the Al_{15} HEA is likely due to the coarse microstructure observed via SEM and TEM, Figs. 1 and 4.

The general trend of increased Al content and reduced mass changes can be correlated with the sub-layers of Al_2O_3. It was found that all of the HEAs examined in this study formed an outer Cr_2O_3 scale. However, increased Al concentration led to increased

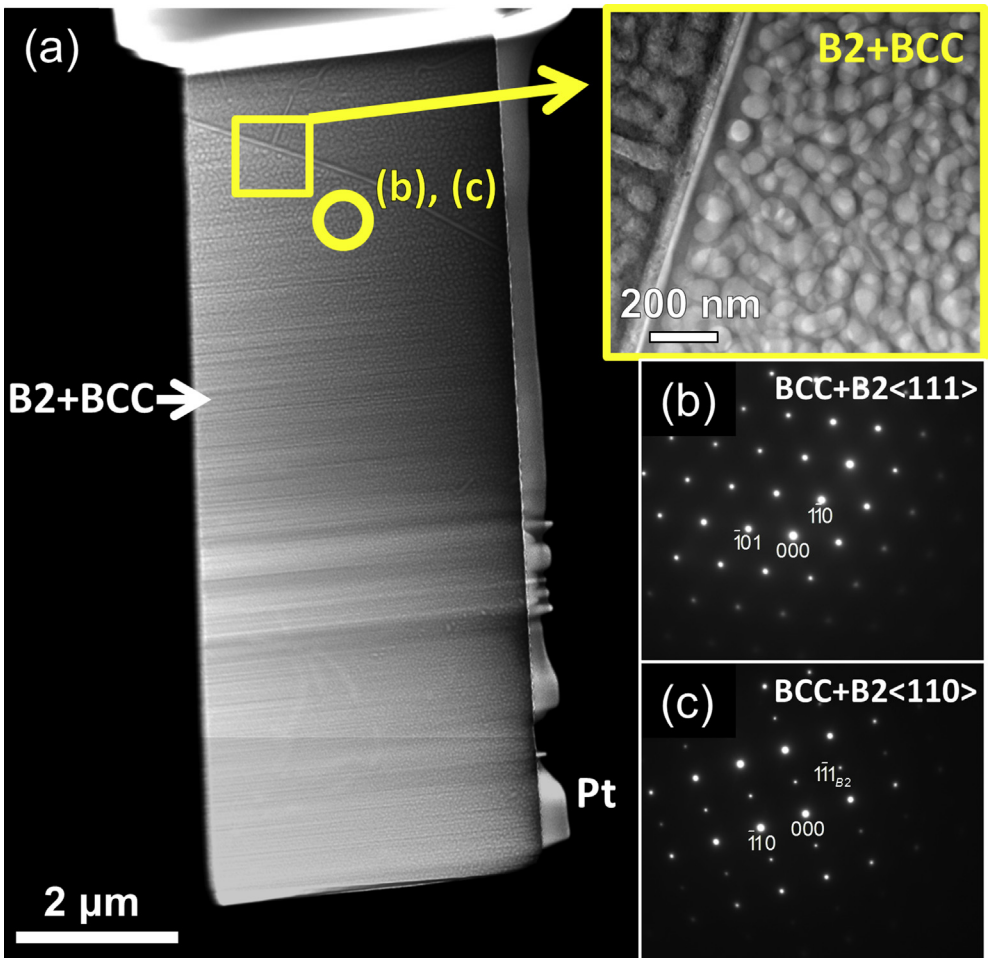

Fig. 6. Microstructure of the as-cast Al_{30} HEA: Mosaic STEM-HAADF image of the specimen lifted out across a grain boundary (a), and corresponding SADPs (b)–(c). The enclosed circles represent where the SADPs were captured from for each phase.

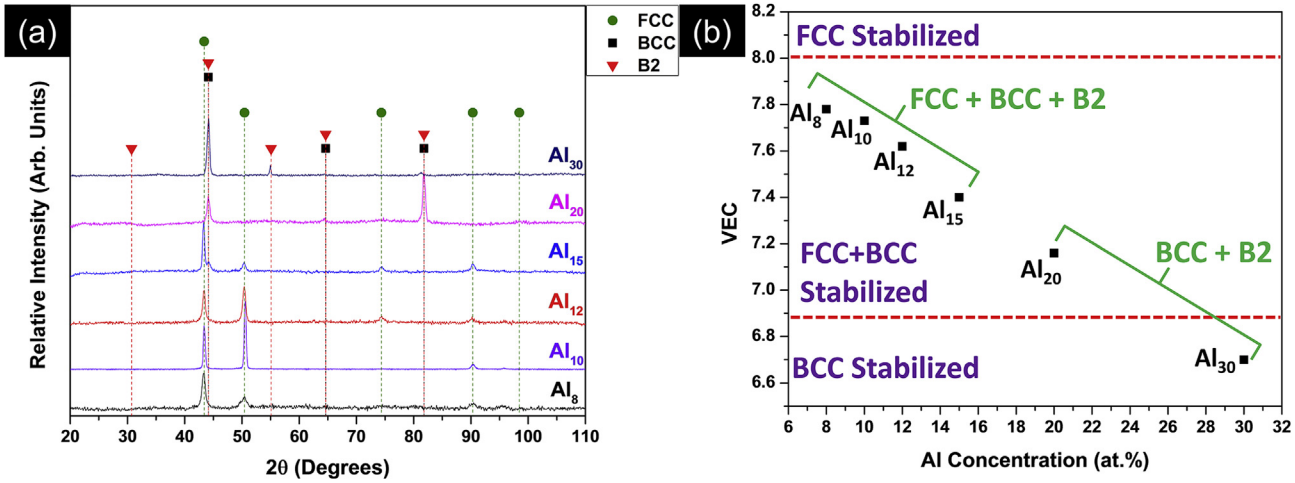

Fig. 7. XRD spectra of the as-cast HEAs with the dominant FCC and BCC peaks identified (a) and plot of valence electron concentration (VEC) vs. Al concentration for the HEAs in this study (b).

continuity of the underlying Al_2O_3 subscale. It was also found to modify the location of Al_2O_3 formation. It is expected that the combination of these two factors enhanced the oxidation resistance in the higher Al content alloys.

3.6. Comparison with conventional oxidation-resistant alloys

High-temperature, oxidation resistant materials rely on the formation of protective oxide scales in order to maintain their

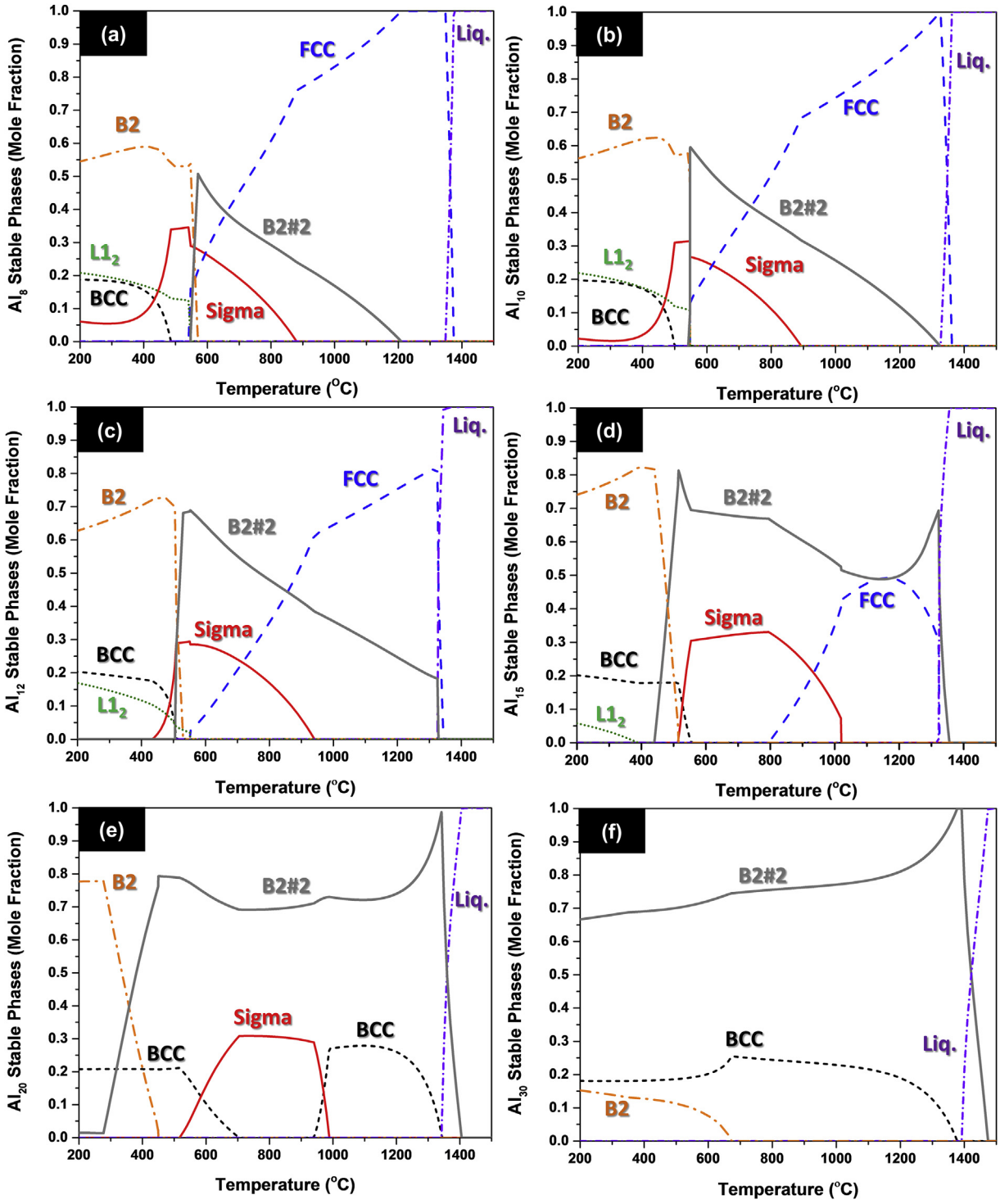

Fig. 8. Thermodynamically calculated phase diagrams for the Al_8 (a), Al_{10} (b), Al_{12} (c), Al_{15} (d), Al_{20} (e), and Al_{30} (f) HEAs. The calculations were performed using the CALPHAD method and TCNI8 database in ThermoCalc.

structural integrity during use. They also exhibit thermally stable internal microstructures, which sustain their expected mechanical abilities. In the present study, all of the HEAs exhibit some of these characteristics. However, in order to effectively design novel alloys for commercial use, it is useful to compare them to conventional materials. The microstructures and oxidation behaviors of the HEAs in this study are quite similar to those found in ternary Ni–Cr–Al alloys and in a variety of alumina-forming austenitic (AFA) stainless steels [28,49,50,57–61].

In particular, the oxidation behaviors of ternary Ni–Cr–Al alloys can be categorized into three different groups. Group I alloys contain limited amounts of Cr and Al, thus inhibiting the formation of protective Cr_2O_3 and Al_2O_3 scales. In this case, non-protective NiO and spinel-type phases form, along with some internal oxidation of Al. Group II alloys contain higher concentrations of Cr, but a limited amount of Al which facilitates the formation of an

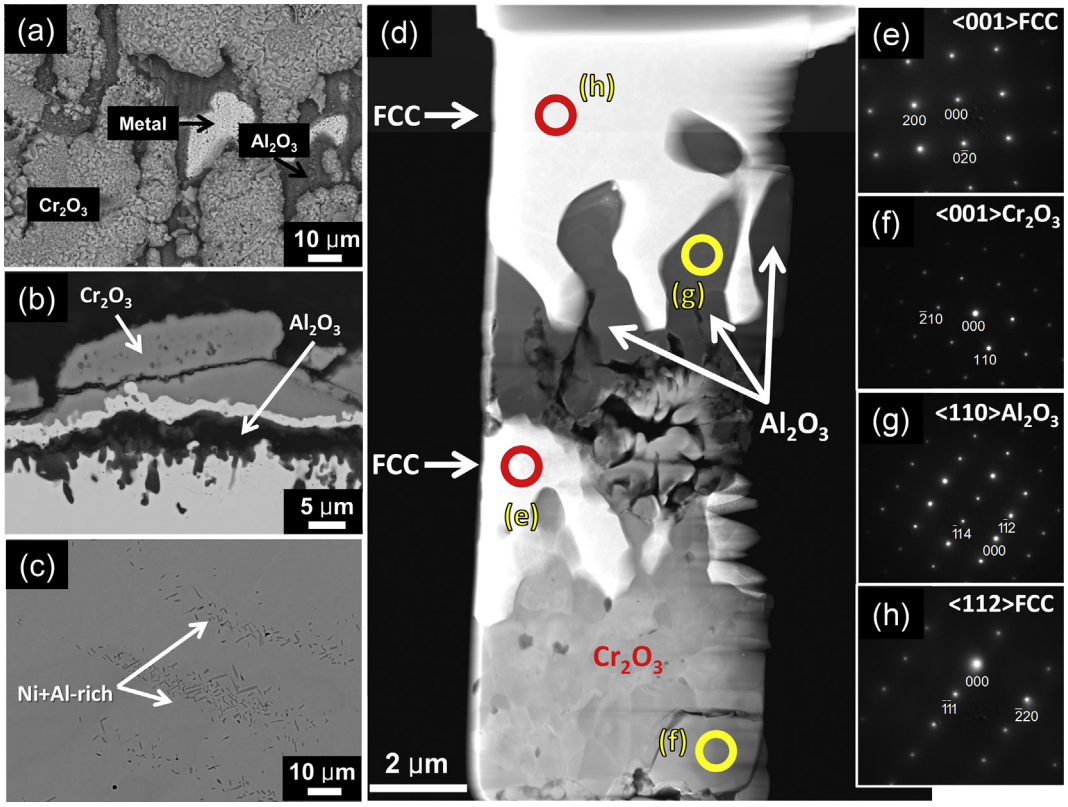

Fig. 9. Plan-view, cross-sectional, and internal backscattered electron images of the Al_8 HEA after 50 h of oxidation at 1050 °C in air (a)–(c), respectively; and mosaic STEM-HAADF image (d) with corresponding SADPs (e)–(h). The enclosed circles denote where diffraction patterns were collected from.

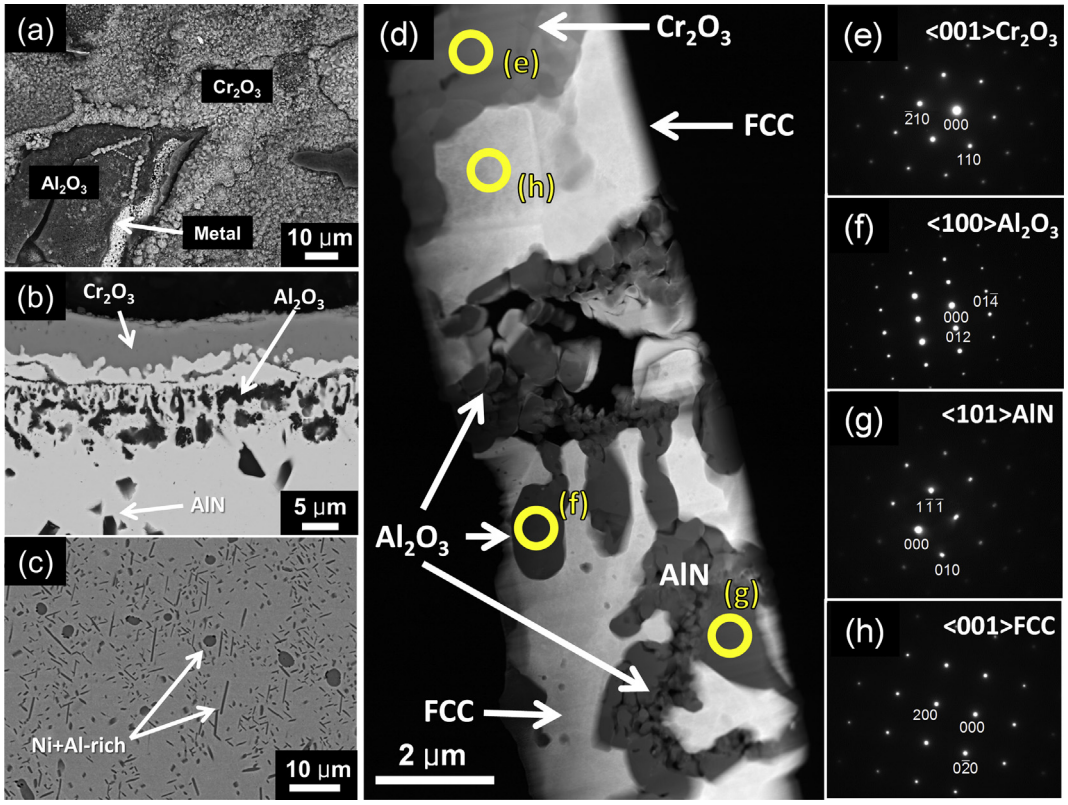

Fig. 10. Plan-view, cross-sectional, and internal backscattered electron images of the Al_{10} HEA after 50 h of oxidation at 1050 °C in air (a)–(c), respectively; and mosaic STEM-HAADF image (d) with corresponding SADPs (e)–(h). The enclosed circles denote where diffraction patterns were collected from.

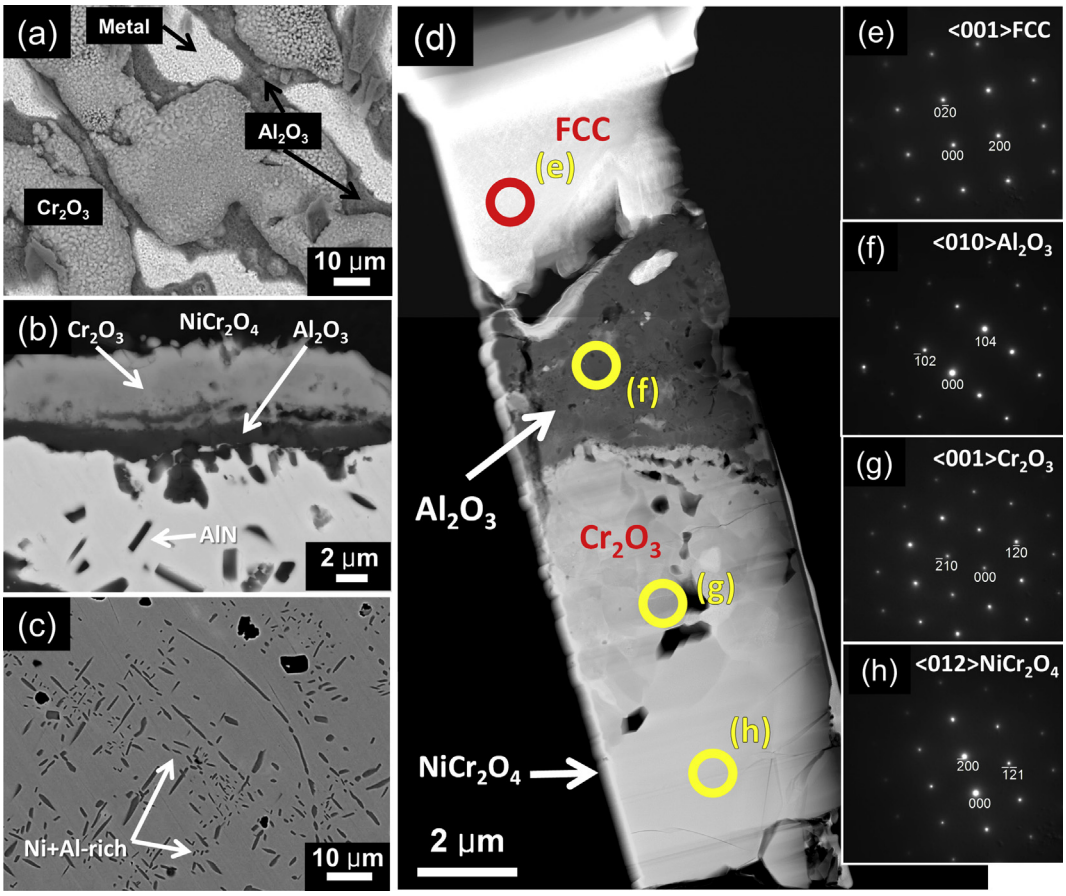

Fig. 11. Plan-view, cross-sectional, and internal backscattered electron images of the Al_{12} HEA after 50 h of oxidation at 1050 °C in air (a)–(c), respectively; and mosaic STEM-HAADF image (d) with corresponding SADPs (e)–(h). The enclosed circles denote where diffraction patterns were collected from.

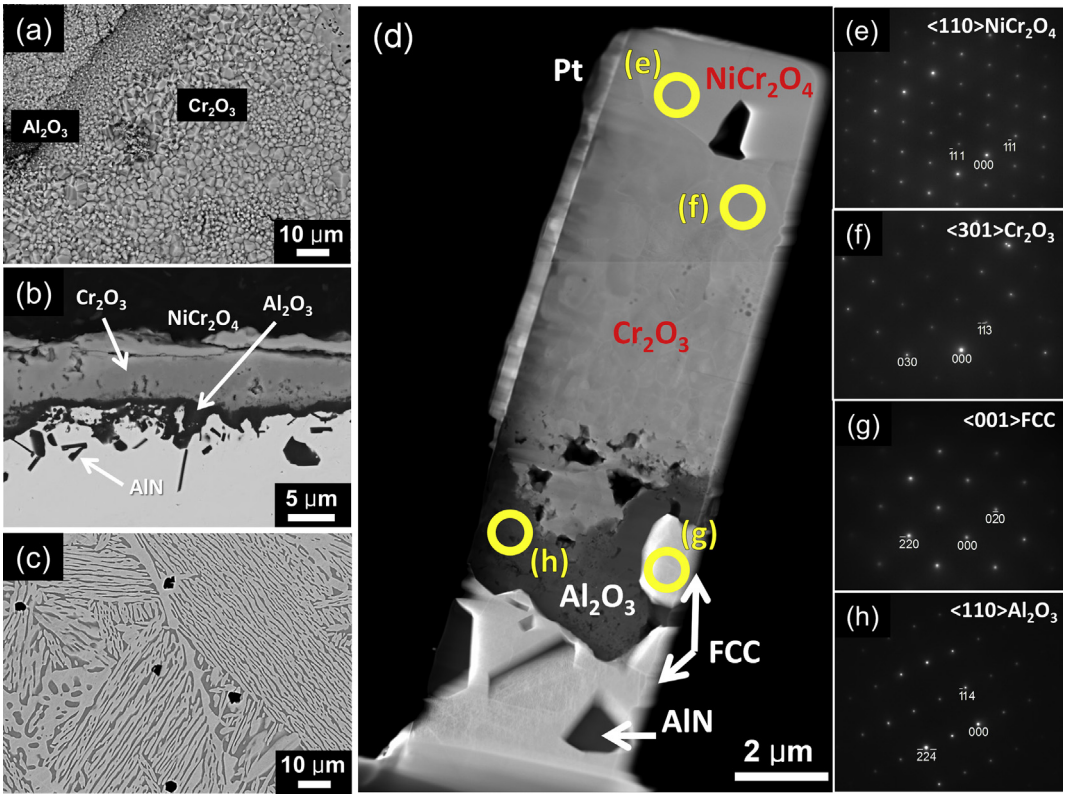

Fig. 12. Plan-view, cross-sectional, and internal backscattered electron images of the Al_{15} HEA after 50 h of oxidation at 1050 °C in air (a)–(c), respectively; and mosaic STEM-HAADF image (d) with corresponding SADPs (e)–(h). The enclosed circles denote where diffraction patterns were collected from.

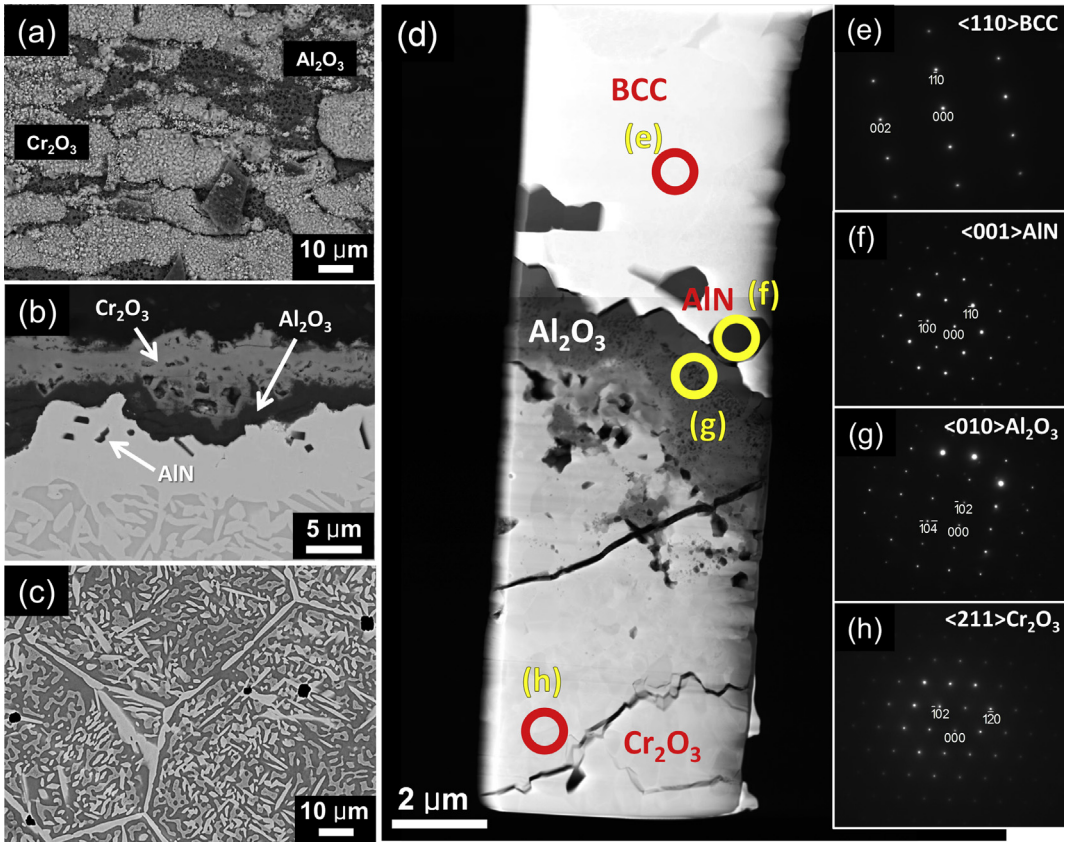

Fig. 13. Plan-view, cross-sectional, and internal backscattered electron images of the Al_{20} HEA after 50 h of oxidation at 1050 °C in air (a)–(c), respectively; and mosaic STEM-HAADF image (d) with corresponding SADPs (e)–(h). The enclosed circles denote where diffraction patterns were collected from.

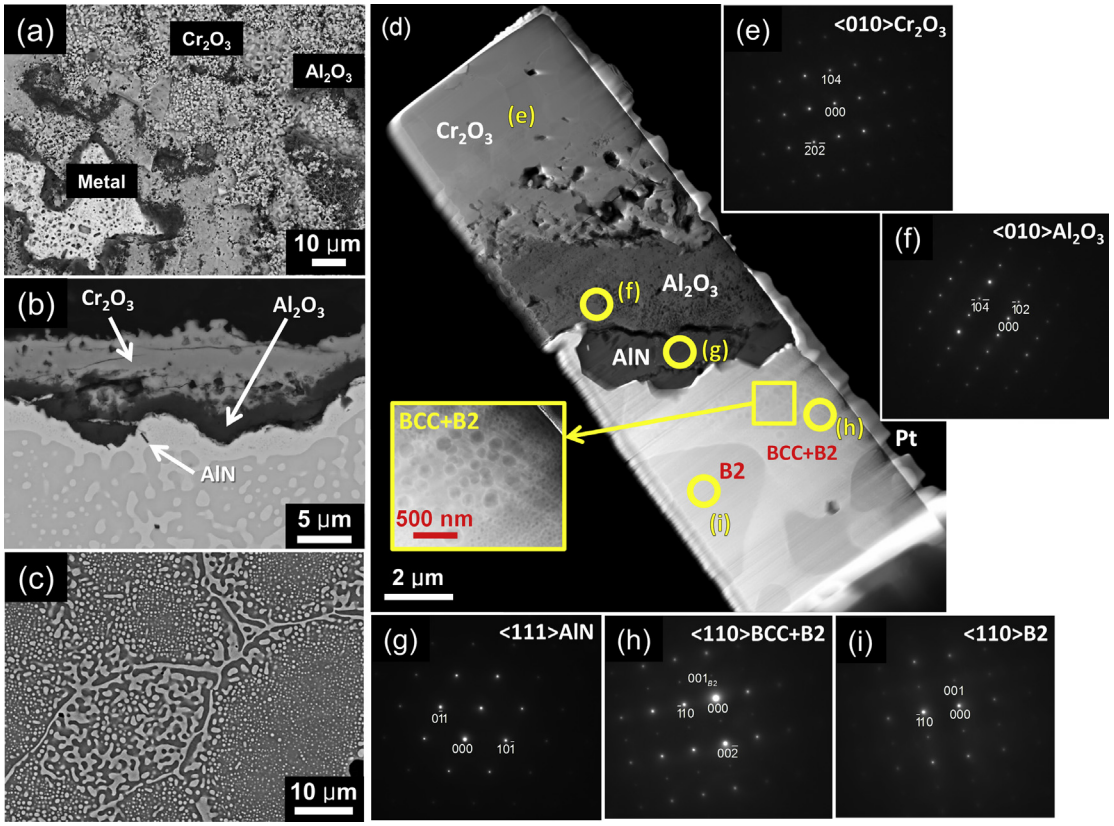

Fig. 14. Plan-view, cross-sectional, and internal backscattered electron images of the Al_{30} HEA after 50 h of oxidation at 1050 °C in air (a)–(c), respectively; and mosaic STEM-HAADF image (d) with corresponding SADPs (e)–(i). The enclosed circles denote where diffraction patterns were collected from.

Table 2
Chemical compositions of the internal phases found in the oxidized alloys along with the calculated entropy of mixing for each phase.

Alloy	Phase	Al	Cr	Fe	Co	Ni	ΔS_{mix} (J/mole × K)	High entropy (>1.5R)
Al_8	Depleted Zone	0.6 ± 0.1	19.7 ± 0.8	26.4 ± 0.9	26.4 ± 0.4	26.9 ± 0.4	11.70	–
	High-Z	6.9 ± 0.4	24.5 ± 0.2	23.4 ± 0.3	23.3 ± 0.1	21.9 ± 0.3	12.81	X
	Low-Z	24.8 ± 2.5	13.6 ± 1.9	14.9 ± 1.2	17.1 ± 0.7	29.6 ± 1.3	13.00	X
Al_{10}	Depleted Zone	0.6 ± 0.1	19.9 ± 0.4	26.3 ± 0.1	25.8 ± 0.3	27.5 ± 0.5	11.70	–
	High-Z	7.1 ± 0.1	24.6 ± 0.1	23.4 ± 0.2	22.7 ± 0.2	22.3 ± 0.2	12.83	X
	Low-Z	24.0 ± 0.7	13.4 ± 0.9	14.4 ± 0.6	16.8 ± 0.2	31.4 ± 0.9	12.92	X
Al_{12}	Depleted Zone	0.9 ± 0.3	19.5 ± 0.1	26.9 ± 0.3	26.1 ± 0.8	26.5 ± 1.5	11.81	–
	High-Z	10.4 ± 0.2	25.1 ± 0.1	20.3 ± 0.4	20.8 ± 0.2	23.4 ± 0.1	13.08	X
	Low-Z	28.3 ± 0.3	10.4 ± 0.2	12.5 ± 0.1	15.7 ± 0.1	33.1 ± 0.6	12.55	X
Al_{15}	Depleted Zone	5.1 ± 0.4	19.2 ± 0.8	23.5 ± 0.3	23.1 ± 1.1	29.1 ± 2.7	12.52	X
	High-Z	6.9 ± 0.2	26.8 ± 0.1	25.2 ± 0.2	23.3 ± 0.2	17.8 ± 0.2	12.73	X
	Low-Z	30.7 ± 0.9	9.8 ± 1.2	12.3 ± 0.8	16.8 ± 0.3	30.5 ± 1.4	12.55	X
Al_{20}	Depleted Zone	5.8 ± 0.5	24.4 ± 0.3	24.7 ± 0.3	21.7 ± 0.2	23.5 ± 0.7	12.68	X
	High-Z	8.4 ± 0.1	25.7 ± 0.5	26.2 ± 0.3	23.4 ± 0.1	16.3 ± 0.7	12.83	X
	Low-Z	31.0 ± 0.3	9.1 ± 0.1	12.9 ± 0.3	18.0 ± 0.1	28.9 ± 0.1	12.58	X
Al_{30}	Depleted Zone	6.9 ± 0.9	36.7 ± 0.3	26.4 ± 0.6	14.4 ± 0.2	15.5 ± 2.0	12.25	–
	High-Z	18.4 ± 0.8	30.8 ± 2.2	23.7 ± 0.9	16.1 ± 1.1	11.1 ± 1.2	12.91	X
	Low-Z	29.1 ± 0.4	17.7 ± 0.6	17.1 ± 0.4	18.1 ± 0.7	17.9 ± 0.6	13.18	X

external Cr_2O_3 scale with an internal subscale of Al_2O_3. Group III alloys, which are the most oxidation resistant, contain higher concentrations of Cr and Al which promotes the formation of a highly-protective external Al_2O_3 scale either with or without minor Cr_2O_3. Based on the microstructural analysis in this work, the oxidized Al_8 and Al_{10} HEAs resemble a Group II Ni–Cr–Al alloy due to the formation of an external Cr_2O_3 scale with an internal, discontinuous Al_2O_3 subscale [50,62]. The oxidized Al_{12} and Al_{15} HEAs exhibit microstructures in between a Group II and Group III Ni–Cr–Al alloy, since they display external Cr_2O_3 along with a semi-discontinuous Al_2O_3 scale. The high Al content HEAs, Al_{20} and Al_{30}, exhibit microstructures consistent with Group III Ni–Cr–Al alloys since they form an external layer of Cr_2O_3 with an underlying, continuous layer of Al_2O_3. In correlation with the Ni–Cr–Al system, it is no surprise that these high Al content HEAs display enhanced oxidation resistances.

Considering a (Ni + Co + Fe)–Cr–Al alloy arrangement, the typical Group I, II, and III zones are plotted along with the HEAs from this study on a schematic oxide formation map in Fig. 16 (b) [50,60–62]. Consistent with the experimental observations, the Al_8 and Al_{10} HEAs sit nearly inside of Group II. The Al_{12} and Al_{15} HEAs sit near the boundary between Groups II and III. Likewise, the Al_{20} and Al_{30} HEAs sit well within Group III. With regard to the parabolic rate constants, k_P, all of the HEAs were in the range of 10^{-11} to 10^{-13} (g^2/cm^4 s), which is equivalent to the ranges observed for Groups II and III Ni–Cr–Al alloys at 1050 °C, Table 3 [50].

The HEAs in this study also share close similarities with AFA stainless steels [58,59,63]. These are stainless steels that alternatively form Al_2O_3 scales in oxygen-containing environments providing protection at temperatures of ~600–900 °C [59]. Similar to the findings in this paper, they observed that some of the oxidized AFA stainless steels formed an outer oxide layer enriched in Al, Cr, Fe, Mn, and Nb, with a continuous internal layer of Al_2O_3. All of the oxidation testing was performed below 900 °C, which inhibits a direct quantitative comparison. These temperatures are well below the oxidation temperature examined in the present study; however, AlNiCoCrFe HEAs share very similar oxidation characteristics but potentially have applicability at higher temperatures. Also, some of the internal microstructures of the AFAs were found to decompose post-oxidation in a manner similar to the Al_8–Al_{12} HEAs.

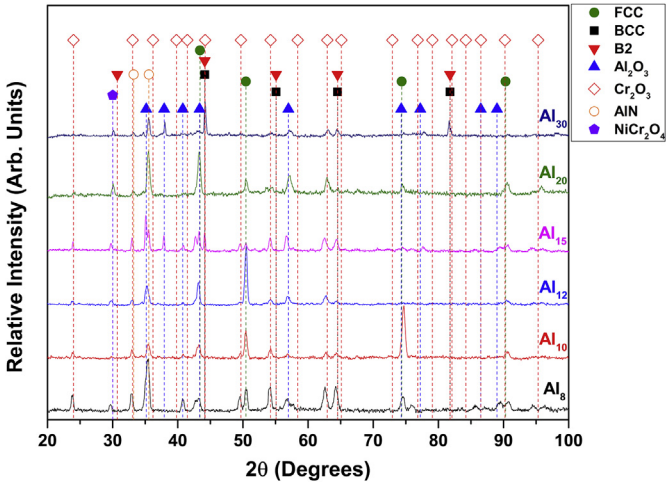

Fig. 15. XRD spectra of the HEAs after 50 h of oxidation at 1050 °C in air.

3.7. Comments on high-entropy and the oxidation behavior of HEAs

Much work that remains to fully understand the influence of high-entropy on the oxidation behavior of HEAs. This study does show that HEAs consisting of Al, Co, Cr, Fe, and Ni tend to oxidize in a similar fashion when compared to Ni–Cr–Al alloys and AFA stainless steels. It also demonstrates the merit of existing oxide formation models for predicting the behavior in more compositionally complex alloys. However, the actual influence of high-entropy on the oxidation behavior remains inconclusive. With regard to the HEAs in this work, the phases formed internally during oxidation, along with their ideal calculated entropies of mixing are shown in Table 2. Aside from several of the depleted zones exhibiting medium entropy, all of the other internal phases remain high in entropy. This infers that the internal microstructures of the oxidized AlCoCrFeNi-based HEAs should still benefit from enhanced mechanical strength and sufficient oxidation/corrosion resistances even after high temperature exposure at 1050 °C. This is a favorable characteristic for materials used in high-temperature structural applications. In order to fully evaluate the influence of high-entropy on the oxidation behavior of HEAs, diffusion-based experiments are needed to determine the relative diffusivities of elements during oxidation as are experiments on well-annealed

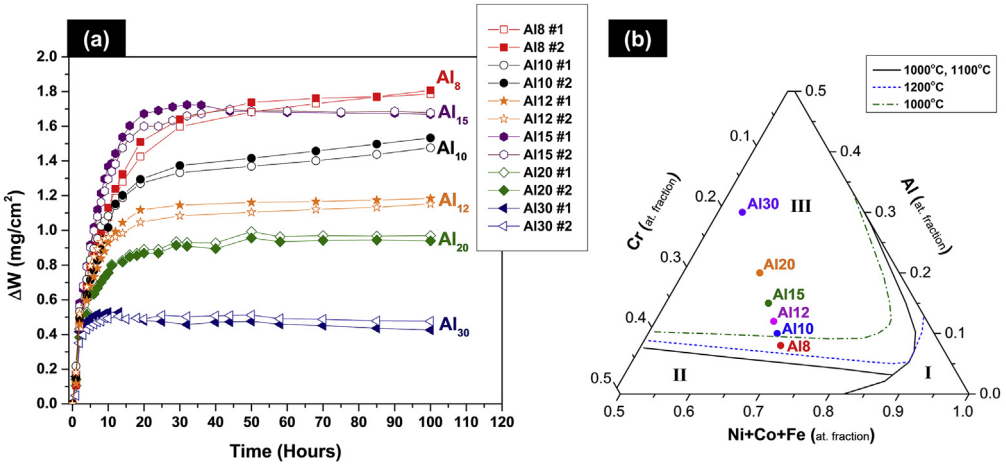

Fig. 16. Relative mass change with time for the 1050 °C oxidized HEAs investigated in this study (a), and schematic oxide map for the Ni–Cr–Al system at 1000 °C, 1100 °C, and 1200 °C [50,60–62] (b).

Table 3
Parabolic oxide growth rate constants calculated for the HEAs in this study.

Alloy	k_P (1) (g^2/cm^4 s)	Adherence duration for k_P (1)	k_P (2) (g^2/cm^4 s)	Adherence duration for k_P (2)	Primary oxides formed	Examination method
Al_8	~2.5×10^{-11}	1–30 h	~2.5×10^{-12}	30–100 h	Cr_2O_3 w/discont. internal Al_2O_3	SEM/TEM
Al_{10}	~2.4×10^{-11}	1–19 h	~1.8×10^{-12}	19–100 h	Cr_2O_3 w/discont. internal Al_2O_3	SEM/TEM
Al_{12}	~1.9×10^{-12}	1–19 h	~4.6×10^{-13}	19–100 h	Cr_2O_3 w/semi-cont. internal Al_2O_3	SEM/TEM
Al_{15}	~4.7×10^{-11}	2–18 h	~4.2×10^{-12}	19–36 h	Cr_2O_3 w/semi-cont. internal Al_2O_3	SEM/TEM
Al_{20}	~8.1×10^{-12}	1–11 h	~1.6×10^{-12}	12–50 h	Cr_2O_3 w/cont. internal Al_2O_3	SEM/TEM
Al_{30}	~1.9×10^{-12}	2–10 h	–	–	Cr_2O_3 w/cont. internal Al_2O_3	SEM/TEM

alloys. In that manner, a conclusive and quantitative measure of the influence of the high-entropy effect on oxidation can be made.

4. Conclusions

In this study, the as-cast and oxidized microstructures of a series of $Al_x(NiCoCrFe)_{100-x}$ HEAs where x = 8, 10, 12, 15, 20, and 30 (at.%) were investigated. The following conclusions can be made:

1) The as-cast Al_8, Al_{10}, and Al_{12} HEAs exhibited dendritic microstructures consisting of an FCC matrix, with Ni + Al-rich, interdendritic (ID) regions. The ID regions were B2 in structure and contained Cr-rich BCC precipitates. The as-cast Al_{15} HEA exhibited a heavily coarsened microstructure consisting of a mixture of FCC regions and ID regions comprised of a BCC matrix with Ni and Al-rich, B2 precipitates. The as-cast Al_{20} and Al_{30} HEAs were found to consist of BCC precipitates in a Ni and Al-rich, B2 matrix. In general, increased Al content was found to shift the dominant alloy structure from FCC to BCC/B2. These findings are consistent with those reported for similar AlNiCoCrFe and AlNiCoCrFeCu HEAs.
2) Thermodynamic modeling of the as-cast HEAs using the CALPHAD method and TCNI8 database in ThermoCalc™ was in reasonable agreement with the experimental findings. The as-cast microstructures mimicked those predicted at high temperatures in excess of 1000 °C. The thermodynamic models were proven to be useful and reasonably accurate in this work, even in the analysis of non-homogenized, arc-melted alloys.
3) Discontinuous, isothermal oxidation of the HEAs at 1050 °C in air promoted the formation of Cr_2O_3, Al_2O_3, $NiCr_2O_4$, and AlN precipitates. For the low Al content HEAs (Al_8 and Al_{10}), an external layer of Cr_2O_3 formed along with an internal discontinuous Al_2O_3 scale and AlN precipitates. For the intermediate Al content HEAs (Al_{12} and Al_{15}), an outer $NiCr_2O_4$ spinel formed, along with Cr_2O_3, followed by an internal, semi-continuous Al_2O_3 scale, and AlN precipitates. For the high Al content HEAs (Al_{20} and Al_{30}), an outer layer of Cr_2O_3 formed, along with internal, continuous Al_2O_3, with few AlN precipitates. The post-oxidation microstructures were found to be comparable to Ni–Cr–Al alloys and alumina-forming austenitic (AFA) stainless steels. All of the post oxidation microstructures were consistent with those predicted for model Group II and Group III Ni–Cr–Al alloys, as proposed by Giggins and Pettit.
4) All of the HEAs exhibited initial transient oxidation (1–2 h), followed by various degrees of parabolic oxide growth. The parabolic constants (k_P) were found to correlate well with model Group II and Group III Ni–Cr–Al alloys. The Al_{30} HEA exhibited the best oxidation resistance, while the Al_8 was the worst. In general, the increased Al content was found to enhance oxidation resistances by promoting the formation of a continuous Al_2O_3 scale.
5) The direct influence of high-entropy on the oxidation behavior of AlCoCrFeNi HEAs remains inconclusive. However, this work shows that compositionally complex alloys can still oxidize in a selective/favorable fashion. Aside from several of the depleted zones, all of the other internal phases in these HEAs post-oxidation remain high-entropy. Thus, it is proposed that even during high-temperature exposure at 1050 °C, the internal microstructures should still benefit from the enhanced properties inherent to HEAs, making them ideal candidates for high-temperature, structural applications.

Acknowledgment

This work utilized equipment owned by the Central Analytical Facility (CAF), which is housed at the University of Alabama.

References

[1] D.B. Miracle, J.D. Miller, O.N. Senkov, C. Woodward, M.D. Uchic, J. Tiley, Exploration and development of high entropy alloys for structural applications, Entropy 16 (2014) 494–525.
[2] S. Guo, C.T. Liu, Phase stability in high entropy alloys: formation of solid-solution phase or amorphous phase, Prog. Nat. Sci. Mater. Int. 21 (2011) 433–446.
[3] A.K. Singh, A. Subramaniam, On the formation of disordered solid solutions in multi-component alloys, J. Alloys Compd. 587 (2014) 113–119.
[4] J.-W. Yeh, Alloy design strategies and future trends in high-entropy alloys, JOM 65 (2013) 1759–1771.
[5] Y. Zhang, T.T. Zuo, Z. Tang, M.C. Gao, K.A. Dahmen, P.K. Liaw, Z.P. Lu, Microstructures and properties of high-entropy alloys, Prog. Mater. Sci. 61 (2014) 1–93.
[6] S. Guo, C. Ng, J. Lu, C.T. Liu, Effect of valence electron concentration on stability of fcc or bcc phase in high entropy alloys, J. Appl. Phys. 109 (2011), 103505(1–5).
[7] Z. Tang, L. Huang, W. He, P.K. Liaw, Alloying and processing effects on the aqueous corrosion behavior of high-entropy alloys, Entropy 16 (2014) 895–911.
[8] S.-Y. Chang, C.-E. Li, Y.-C. Huang, H.-F. Hsu, J.-W. Yeh, S.-J. Lin, Structural and thermodynamic factors of suppressed interdiffusion kinetics in multi-component high-entropy materials, Sci. Rep. 4 (2014) 4162.
[9] D.L. Beke, G. Erdélyi, On the diffusion in high-entropy alloys, Mater. Lett. 164 (2016) 111–113.
[10] K.Y. Tsai, M.H. Tsai, J.W. Yeh, Sluggish diffusion in Co–Cr–Fe–Mn–Ni high-entropy alloys, Acta Mater. 61 (2013) 4887–4897.
[11] P.K. Huang, J.W. Yeh, T.T. Shun, S.K. Chen, Multi-principal-element alloys with improved oxidation and wear resistance for thermal spray coating, Adv. Eng. Mater. 6 (2004) 74–78.
[12] C.M. Liu, H.M. Wang, S.Q. Zhang, H.B. Tang, A.L. Zhang, Microstructure and oxidation behavior of new refractory high entropy alloys, J. Alloys Compd. 583 (2014) 162–169.
[13] H. Zhang, Q.T. Wang, Q.H. Tang, P.Q. Dai, High temperature oxidation property of $Al_{0.5}FeCoCrNi(Si_{0.2}$, $Ti_{0.5})$ high entropy alloys, Corros. Prot. 34 (2013) 561–565.
[14] O.N. Senkov, S.V. Senkova, D.M. Dimiduk, C. Woodward, D.B. Miracle, Oxidation behavior of a refractory $NbCrMo_{0.5}Ta_{0.5}TiZr$ alloy, J. Mater. Sci. 47 (2012) 6522–6534.
[15] C. Huang, Y. Zhang, J. Shen, R. Vilar, Thermal stability and oxidation resistance of laser clad TiVCrAlSi high entropy alloy coatings on Ti-6Al-4V alloy, Surf. Coat. Technol. 206 (2011) 1389–1395.
[16] S.-T. Chen, W.-Y. Tang, Y.-F. Kuo, S.-Y. Chen, C.-H. Tsau, T.-T. Shun, J.-W. Yeh, Microstructure and properties of age-hardenable $Al_xCrFe_{1.5}MnNi_{0.5}$ alloys, Mater. Sci. Eng. A 527 (2010) 5818–5825.
[17] M.-H. Chuang, M.-H. Tsai, W.-R. Wang, S.-J. Lin, J.-W. Yeh, Microstructure and wear behavior of AlxCo1.5CrFeNi1.5Tiy high-entropy alloys, Acta Mater. 59 (2011) 6308–6317.
[18] C.-C. Juan, C.-Y. Hsu, C.-W. Tsai, W.-R. Wang, T.-S. Sheu, J.-W. Yeh, S.-K. Chen, On microstructure and mechanical performance of $AlCoCrFeMo_{0.5}Ni_x$ high-entropy alloys, Intermetallics 32 (2013) 401–407.
[19] Y. Zhang, X. Yang, P.K. Liaw, Alloy design and properties optimization of high-entropy alloys, JOM 64 (2012) 830–838.
[20] H. Duan, Y. Wu, M. Hua, C. Yuan, D. Wang, J. Tu, H. Kou, J. Li, Tribological properties of AlCoCrFeNiCu high-entropy alloys in hydrogen peroxide solution and in oil lubricant, Wear 297 (2013) 1045–1051.
[21] J.C. Huang, Evaluation of tribological behavior of Al-Co-Cr-Fe-Ni high entropy alloys using molecular dynamics simulation, Scanning 34 (2012) 325–331.
[22] N.T.B.N. Koundinya, C.S. Babu, K. Sivaprasad, P. Susila, N.K. Babu, J. Baburao, Phase evolution and thermal analysis of nanocrystalline AlCrCuFeNiZn high entropy alloy produced by mechanical alloying, J. Mater. Eng. Perform. 22 (2013) 3077–3084.
[23] T.M. Butler, J.P. Alfano, R.L. Martens, M.L. Weaver, High-temperature oxidation behavior of Al-Co-Cr-Ni-(Fe or Si) multicomponent high-entropy alloys, JOM 67 (2015) 246–259.
[24] B. Gorr, M. Azim, H.J. Christ, T. Mueller, D. Schliephake, M. Heilmaier, Phase equilibria, microstructure, and high temperature oxidation resistance of novel refractory high-entropy alloys, J. Alloys Compd. 624 (2015) 270–278.
[25] J. Jiang, X. Luo, High temperature oxidation behaviour of AlCuTiFeNiCr high-entropy alloy, Adv. Mater. Res. 652–654 (2013) 1115–1118.
[26] H.M. Daoud, A.M. Manzoni, R. Volkl, N. Wanderka, U. Glatzel, Oxidation behavior of $Al_8Co_{17}Cr_{17}Cu_8Fe_{17}Ni_{33}$, $Al_{23}Co_{15}Cr_{23}Cu_8Fe_{15}Ni_{15}$, and $Al_{17}Co_{17}Cr_{17}Cu_{17}Fe_{17}Ni_{17}$ compositionally complex alloys (high-entropy alloys) at elevated temperatures in Air, Adv. Eng. Mater. 17 (2015) 1134–1141.
[27] G.R. Holcomb, J. Tylczak, C. Carney, Oxidation of CoCrFeMnNi high entropy alloys, JOM 67 (2015) 2326–2339.
[28] Y.-x. Liu, C.-q. Cheng, J.-l. Shang, R. Wang, P. Li, J. Zhao, Oxidation behavior of high-entropy alloys $Al_xCoCrFeNi$ (x=0.15, 0.4) in supercritical water and comparison with HR3C steel, Trans. Nonferrous Metals Soc. China 25 (2015) 1341–1351.
[29] H.H. Yang, W.T. Tsai, J.C. Kuo, Effect of pre-oxidation on increasing resistance of Fe-Al-Ni-Cr-Co-Mn high entropy alloys to molten Al attack, Corros. Eng. Sci. Technol. 49 (2014) 124–129.
[30] D. Tomus, H.P. Ng, In situ lift-out dedicated techniques using FIB–SEM system for TEM specimen preparation, Micron 44 (2013) 115–119.
[31] ES Vision Software, FEI-Company, Hillsboro, OR, 2004.
[32] ThermoCalc Software Package, Version 2015a, ThermoCalc Software AB, Stockholm, Sweden, 2015.
[33] TCNI8-TCS Ni-based Superalloys Database, Version 8.0, ThermoCalc Software AB, Stockholm, Sweden, 2015.
[34] Z.P. Lu, H. Wang, M.W. Chen, I. Baker, J.W. Yeh, C.T. Liu, T.G. Nieh, An assessment on the future development of high-entropy alloys: summary from a recent workshop, Intermetallics 66 (2015) 67–76.
[35] Q.H. Tang, Y. Huang, Y.Y. Huang, X.Z. Liao, T.G. Langdon, P.Q. Dai, Hardening of an Al0.3CoCrFeNi high entropy alloy via high-pressure torsion and thermal annealing, Mater. Lett. 151 (2015) 126–129.
[36] Z. Tang, O.N. Senkov, C.M. Parish, C. Zhang, F. Zhang, L.J. Santodonato, G. Wang, G. Zhao, F. Yang, P.K. Liaw, Tensile ductility of an AlCoCrFeNi multi-phase high-entropy alloy through hot isostatic pressing (HIP) and homogenization, Mater. Sci. Eng. A 647 (2015) 229–240.
[37] W.-R. Wang, W.-L. Wang, S.-C. Wang, Y.-C. Tsai, C.-H. Lai, J.-W. Yeh, Effects of Al addition on the microstructure and mechanical property of $Al_xCoCrFeNi$ high-entropy alloys, Intermetallics 26 (2012) 44–51.
[38] W.-R. Wang, W.-L. Wang, J.-W. Yeh, Phases, microstructure and mechanical properties of $Al_xCoCrFeNi$ high-entropy alloys at elevated temperatures, J. Alloys Compd. 589 (2014) 143–152.
[39] Y.P. Wang, B.S. Li, M.X. Ren, C. Yang, H.Z. Fu, Microstructure and compressive properties of AlCrFeCoNi high entropy alloy, Mater. Sci. Eng. A 491 (2008) 154–158.
[40] M.V. Ivchenko, V.G. Pushin, N. Wanderka, High-entropy equiatomic AlCrFeCoNiCu alloy: hypotheses and experimental data, Tech. Phys. 59 (2014) 211–223.
[41] V.M. Nadutov, S.Y. Makarenko, P.Y. Volosevich, Effect of aluminum on fine structure and distribution of chemical elements in high-entropy alloys Al_x-FeNiCoCuCr, Phys. Metals Metallogr. 116 (2015) 439–444.
[42] S. Singh, N. Wanderka, K. Kiefer, K. Siemensmeyer, J. Banhart, Effect of decomposition of the Cr–Fe–Co rich phase of AlCoCrCuFeNi high entropy alloy on magnetic properties, Ultramicroscopy 111 (2011) 619–622.
[43] C.-J. Tong, Y.-L. Chen, J.-W. Yeh, S.-J. Lin, S.-K. Chen, T.-T. Shun, C.-H. Tsau, S.-Y. Chang, Microstructure characterization of AlxCoCrCuFeNi high-entropy alloy system with multiprincipal elements, Metall. Mater. Trans. A 36 (2005) 881–893.
[44] A. Manzoni, H. Daoud, S. Mondal, S. van Smaalen, R. Völkl, U. Glatzel, N. Wanderka, Investigation of phases in Al23Co15Cr23Cu8Fe15Ni16 and Al8Co17Cr17Cu8Fe17Ni33 high entropy alloys and comparison with equilibrium phases predicted by Thermo-Calc, J. Alloys Compd. 552 (2013) 430–436.
[45] C. Ng, S. Guo, J. Luan, S. Shi, C.T. Liu, Entropy-driven phase stability and slow diffusion kinetics in an Al0.5CoCrCuFeNi high entropy alloy, Intermetallics 31 (2012) 165–172.
[46] C. Zhang, F. Zhang, S. Chen, W. Cao, Computational thermodynamics aided high-entropy alloy design, JOM 64 (2012) 839–845.
[47] F. Zhang, C. Zhang, S.L. Chen, J. Zhu, W.S. Cao, U.R. Kattner, An understanding of high entropy alloys from phase diagram calculations, Calphad 45 (2014) 1–10.
[48] U. Krupp, H.J. Christ, Selective oxidation and internal nitridation during high-temperature exposure of single-crystalline nickel-base superalloys, Metall. Mater. Trans. A 31 (2000) 47–56.
[49] J. Hall, K. Hellström, J.E. Svensson, M. Norell, M. Lundberg, T. Helander, L.G. Johansson, The initial oxide scale development on a model FeNiCrAl alloy at 900°c in dry and humid atmosphere: a detailed investigation, Oxid. Metals 82 (2014) 225–247.
[50] C.S. Giggins, F.S. Pettit, Oxidation of Ni-Cr-Al alloys between 1000°C and 1200°C, J. Electrochem. Soc. 118 (1971) 1782–1790.
[51] P. Kofstad, High Temperature Corrosion, Elsevier Applied Science, New York, 1988.
[52] J.C. Yang, E. Schumann, I. Levin, M. Rühle, Transient oxidation of NiAl, Acta Mater. 46 (1998) 2195–2201.
[53] Z. Liu, W. Gao, K.L. Dahm, F. Wang, Oxidation behaviour of sputter-deposited Ni–Cr–Al micro-crystalline coatings, Acta Mater. 46 (1998) 1691–1700.
[54] L. Liu, Z.-g. Yang, C. Zhang, M. Ueda, K. Kawamura, T. Maruyama, Effect of grain size on the oxidation of Fe–13Cr–5Ni alloy at 973 K in Ar–21 vol%O_2, Corros. Sci. 91 (2015) 195–202.
[55] C. Jang, D. Kim, D. Kim, I. Sah, W.-S. Ryu, Y.-s. Yoo, Oxidation behaviors of wrought nickel-based superalloys in various high temperature environments, Trans. Nonferrous Metals Soc. China 21 (2011) 1524–1531.
[56] W. Kai, W.L. Jang, R.T. Huang, C.C. Lee, H.H. Hsieh, C.F. Du, Air Oxidation of FeCoNi-Base Equi-Molar Alloys at 800–1000°C, Oxid. Metals 63 (2005) 169–192.
[57] J.E. Croll, G.R. Wallwork, The design of iron-chromium-nickel alloys for use at high temperatures, Oxid. Metals 1 (1969) 55–71.
[58] X. Xu, X. Zhang, G. Chen, Z. Lu, Improvement of high-temperature oxidation resistance and strength in alumina-forming austenitic stainless steels, Mater. Lett. 65 (2011) 3285–3288.
[59] M.P. Brady, Y. Yamamoto, M.L. Santella, P.J. Maziasz, B.A. Pint, C.T. Liu, Z.P. Lu, H. Bei, The development of alumina-forming austenitic stainless steels for high-temperature structural use, JOM 60 (2008) 12–18.
[60] M.W. Brumm, H.J. Grabke, The oxidation behaviour of NiAl-I. phase transformations in the alumina scale during oxidation of NiAl and NiAl-Cr alloys,

Corros. Sci. 33 (1992) 1677–1690.
[61] G.R. Wallwork, A.Z. Hed, Some limiting factors in the use of alloys at high temperatures, Oxid. Metals 3 (1971) 171–184.
[62] N. Birks, G.H. Meier, F.S. Pettit, High-temperature Oxidation of Metals, second ed., Cambridge University Press, Cambridge, UK, 2006.
[63] B.A. Pint, J.P. Shingledecker, M.P. Brady, P.J. Maziasz, Alumina-forming Austenitic Alloys for Advanced Recuperators," in 2007 ASME Turbo Expo, May 14-17 2007, American Society of Mechanical Engineers, New York, NY 10016-5990, United States, Montreal, Que., Canada, 2007, pp. 995–1002.